



Shock wave-Boundary Layer Interactions in Wedge-induced Oblique Detonations

Shikun Miao, Dekun Xu, Tianli Song, and Junjun Yu

College of Aerospace Science and Engineering, National University of Defence Technology, Changsha, Hunan Province, People's Republic of China

ABSTRACT

The flow structure and stability of oblique detonation waves (ODWs) affected by shock wave-boundary layer interactions (SBLIs) are investigated based on Reynolds averaging method. ODWs with smooth and abrupt transitions are studied separately. The results show that there are no shock waves behind detonation wave surface for ODWs with smooth transitions, so the flow structures are only affected by the ramp-induced SBLI. Under the circumstances, the compression effects of the focused shock instead of the separation shock is the main cause of the initiation of ODW, which leads to an obvious increase in the initiation length. In ODWs with abrupt transitions, the primary transverse wave is formed and reflects on the wedge surface. Besides the ramp-induced SBLI, post-wave SBLI also occurs. The two kinds of SBLIs are influenced by the thickness of the inflow boundary layer and the activity of the inflow mixture. When the inflow boundary layer is thin and the activity is low, the separation zone is small and the distance between the ramp-induced separation zone and the post-wave separation zone is large, which makes the ramp-induced separation separated from the post-wave subsonic area. The post-wave SBLI makes the shock configuration at the end of the induction zone change from the λ -shaped to the Y-shaped, which weakens the stability of the ODW. When the inflow boundary layer is thick or the activity is high, the separation zone is large and the distance between the two separation areas is large, which makes the ramp-induced separation merge with the post-wave subsonic area and an extended separation is formed which covers the wedge surface. As the flowfield develops, the extended separation becomes larger and larger, leading to further increase of the initiation length. Finally the ODW propagates out of the calculation domain and fails to be stabilized on the wedge surface.

ARTICLE HISTORY

Received 19 December 2018

Revised 17 June 2019

Accepted 17 July 2019

KEYWORDS

Boundary layer; shock wave-boundary layer interaction; oblique detonation; transition structure; stability

Introduction

Oblique detonation wave engine (ODWE) is a kind of hypersonic propulsion device with simple initiation method, which has been studied for several decades. Because of the higher thermodynamic efficiency and the faster reaction rate, ODWE is considered a proper concept for hypersonic air-breathing propulsion and its feasibility and advantages have been demonstrated in some early studies (Ashford and Emanuel 1996; Kailasanath 2000; Valorani, Digiaccinto, Buongiorno 2001; Wolański 2013). However,

CONTACT Shikun Miao ✉ miaoshikun@nudt.edu.cn 📠 National University of Defence Technology, Changsha, Hunan Province 410073, People's Republic of China

Color versions of one or more of the figures in the article can be found online at www.tandfonline.com/gcst.

© 2019 Taylor & Francis Group, LLC

there are still no practical devices using this kind of combustion by now. At early stage of investigation, the initiation (Maeda et al. 2011; Maeda, Kasahara, Matsuo 2012; Maeda et al. 2013; Teng, Ng, Jiang 2017, 2016; Verreault and Higgins 2011; Wang et al. 2015) and stabilization (Kaneshige and Shepherd 1996; Kasahara et al. 2002; Lefebvre and Fujiwara 1995a; Teng, Zhao, Jiang 2007) of ODWs are always the key problems. After the proposition of the energy limit (Vasiljev 1994) and the kinetic limit (Ju and Sasoh 1997; Verreault and Higgins 2011) of ODW initiation, more attention was paid to the complicated wave structure of ODW.

In early research, the ODW was usually treated as a strong oblique shock with an instantaneous post-shock heat release. Until 1990s, Li et al. (Li, Kailasanath, Oran 1993a) found that an ODW is usually composed of a non-reactive oblique shock, an induction zone, a set of deflagration waves and an oblique detonation wave, where the non-reactive shock is separated from the oblique detonation wave by a triple point. Later, Viguier et al. (Viguier et al. 1996) also found the same structure as Li. However, in the study of Broda (Broda 1993), the non-reactive oblique shock was found to transit to the oblique detonation smoothly without any triple points. Soon afterwards, this kind of structure was validated by other investigations (Vlasenko and Sabel'nikov 1995). Therefore, ODWs are classified as abrupt ODWs or smooth ODWs according to the transition structures, which are shown in Figure 1.

It is shown in Figure 1, the existence of primary transverse wave and primary triple point is the main difference between these two kinds of structure. The formation conditions of different transition structures have been investigated by many scholars and it was found that the transition structure is affected by inflow conditions and wedge angles (Lefebvre and Fujiwara 1995b; Papalexandris 2000). Besides, several quantitative investigations have been carried out and different criteria have been proposed to judge or predict the transition structure (Liu et al. 2018; Miao et al. 2018; Silva and Deshaies 2000; Teng and Jiang 2012; Wang, Zhao, Jiang 2011).

As the studies progress, structures of ODWs with abrupt transitions are found to be more complicated, and some new ODW structures have been observed. Teng et al. (Teng, Zhang, Jiang 2014) studied the ODW structures numerically, and found that when the incident Mach number changes, three kinds of shock configurations, i.e. the λ -shaped shock, X-shaped shock

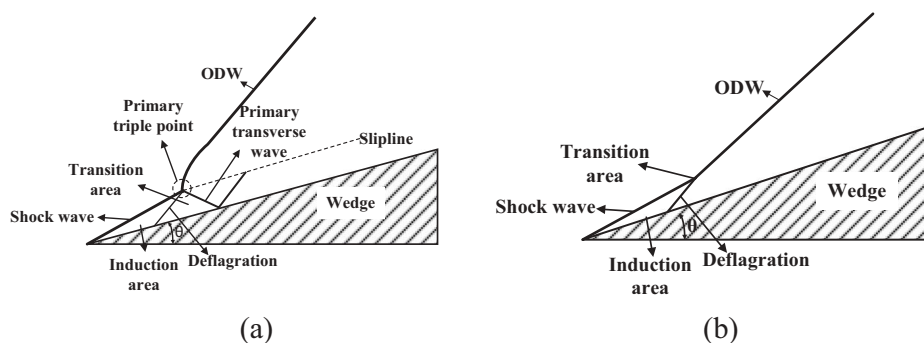


Figure 1. Schematic of ODWs with different transition structures. (a) Abrupt transition structure. (b) Smooth transition structure.

and Y-shaped shock, appear at the end of the induction zone. Liu et al. (Liu et al. 2016) simulated the abrupt transition structures specially. Their results showed that four configurations of the Chapman-Jouguet ODW reflection (overall Mach reflection, Mach reflection, regular reflection, and non-reflection) are observed to take place sequentially as the inflow Mach number increases. Yang et al. (Yang et al. 2017) conducted numerical studies on ODWs induced by semi-infinite cones. In their paper, a novel wave structure was depicted when either the cone angle or incident Mach number is reduced. In this structure, the strong coupling between the shock and the combustion front can be observed at two distinct points. The curvature effect was found to be more dominated for the flow of the conical detonations and the formation of the novel structure.

Then, Yang et al. (Yang et al. 2018) investigated the effects of inflow Mach number on the structure of wedge-induced oblique detonations. It was showed that with the decrease of the inflow Mach number, the wave in the shocked gas may change into a secondary ODW, accompanying an abrupt shift of the main ODW position. Therefore, there exists three topologies of wave structures totally, which are shown in Figure 2. In the new topology, the structural shift is found to be dominated by the main ODW, whose position is sensitive near the critical Mach number.

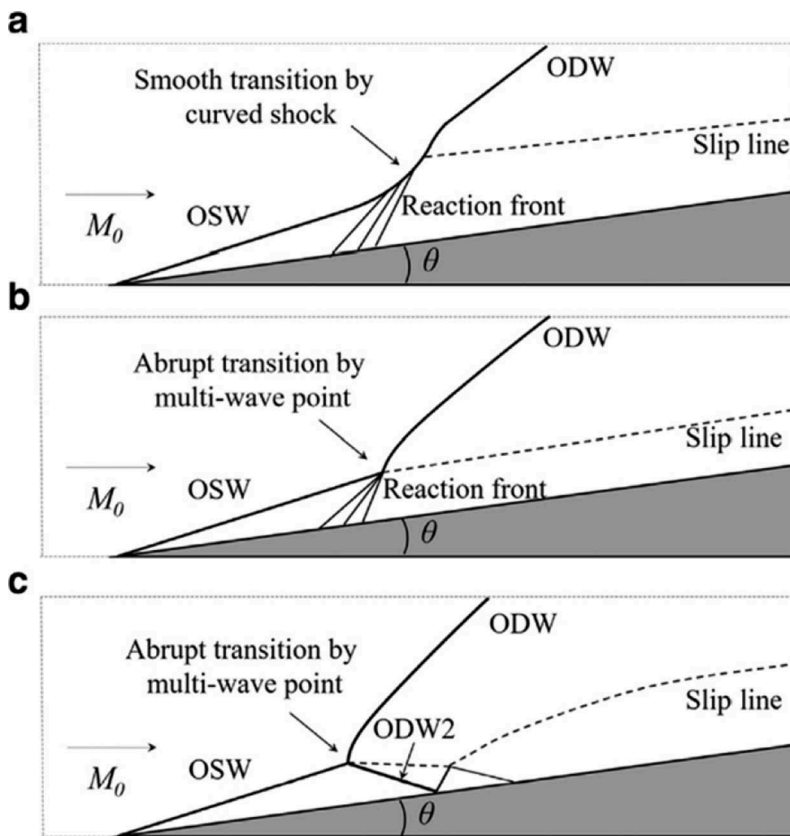


Figure 2. Sketches of the three types of ODW structures in Ref. (Yang et al. 2018).

Actually, most of the studies on ODWs are based on the inviscid assumption, where the effects of boundary layers are neglected. By now, only several studies have been conducted on interactions between detonation waves and boundary layers. Li et al. (Li, Kailasanath, Oran 1993b) may be the first to explore the ODW structure influenced by boundary layer. In their study, post-wave boundary layers were taken into consideration, and it was indicated that the overall detonation structure is very similar to that observed in the inviscid simulations. Afterwards, Choi et al. (Choi and Jeung 2016) conducted numerical simulations on ODWs in a ram accelerator, where the effects of boundary layers were analyzed. It was found that in the confined space, the performance of the ram accelerator is remarkably decreased by the boundary layer, and the stabilizing range of ODWs becomes smaller. Besides, they also indicated that a separation bubble is formed at the origin of oblique detonation and compression waves are formed ahead of this separation bubble. The sketch of this structure is shown in Figure 3. However, the formation condition of the separation bubble and its influence on ODWs were not given in their paper.

Liu et al. (Liu, Zhou, Lin 2014) carried out experimental investigations on the structure and the reflection of ODWs influenced by turbulence boundary layer. It was suggested that the transition structures of ODWs can be affected by the separation of inflow boundary layer. When the separation zone is small, the ODW structure is not affected apparently. However, when the separation zone expands to a moderate size, the transition structure will be abrupt or smooth intermittently. When the separation zone is large enough, the transition structure is likely to be a smooth one. Then, Liu et al. (Liu, Zhou, Lin 2015) conducted numerical investigations which were consistent with the experimental results.

According to the existing studies, the characteristics of ODWs are affected by boundary layers. However, more systematic investigations are still needed, especially on the interaction between ODWs and boundary layers.

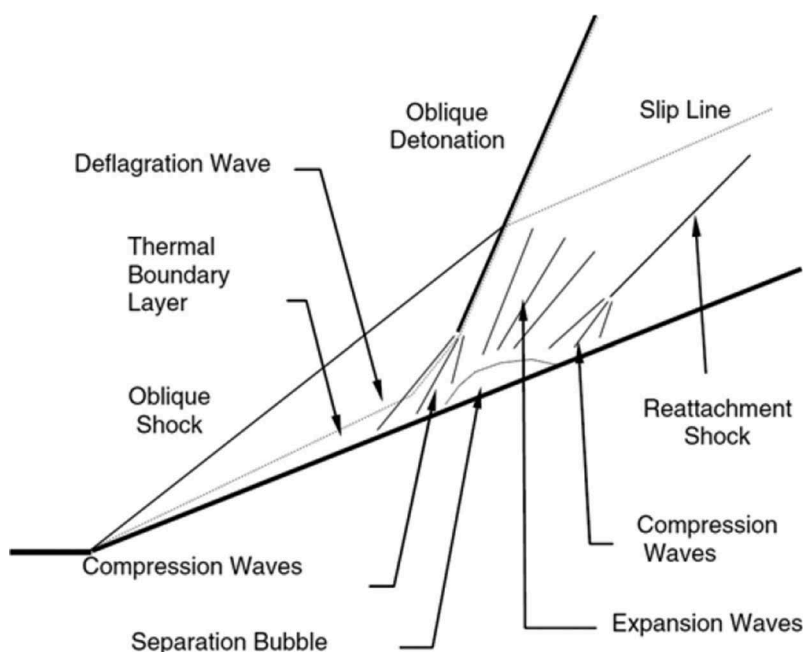


Figure 3. Schematic of stabilized ODW supported by strong shock wave-boundary layer interaction (Choi and Jeung 2016).

In the present paper, numerical simulations investigations are carried out, which are focused on the shock wave-boundary layer interactions (SBLIs) in wedge-induced oblique detonations. Firstly, the numerical method is introduced in section 2, followed by the validation of the numerical method. Then, the effects of boundary layers on ODWs with smooth transitions are investigated in section 4.1. In section 4.2, the SBLI problems in ODWs with abrupt transitions are studied and the stability of ODWs are analyzed.

Mathematical model and numerical method

Mathematical model

The two-dimensional numerical simulations are conducted in a supersonic channel with a fixed wedge, which is shown in Figure 4. The height and the length of the channel are $H = 90$ mm and $X = 160$ mm, respectively. To emphasize the influence of inflow boundary layer, a lengthened parallel channel is set ahead of the fixed wedge, and the distance between the wedge tip and the inlet is $D_1 = 100$ mm. The projected length of the wedge along the x -axis is $D_2 = 60$ mm and the wedge angle is $\theta = 22^\circ$. To mimic a realistic working condition, high-enthalpy supersonic combustible mixtures are selected, which consist of H_2 and Air with a molecular proportion of $H_2: O_2: N_2 = 2 \times ER: 1: 3.76$, where ER is the equivalence ratio. The inflow static pressure and temperature are fixed, i.e., $T_0 = 872$ K, $P_0 = 63$ kPa.

In the simulations, pressure far-field conditions are used in the left and upper boundaries to model a free-stream condition, where the free-stream Mach number, species mass fractions, static conditions. The Reynolds averaging method is utilized in the present paper, where the turbulence parameters are needed. However, laminar boundary layers are focused in the paper, so the turbulence intensity is set to be a very small value, i.e., $I = u'/u_{avg} = 0.001\%$. The no-slip impermeable adiabatic walls with no adsorption of components and no catalytic reactions are used on the lower boundary and the wedge surface.

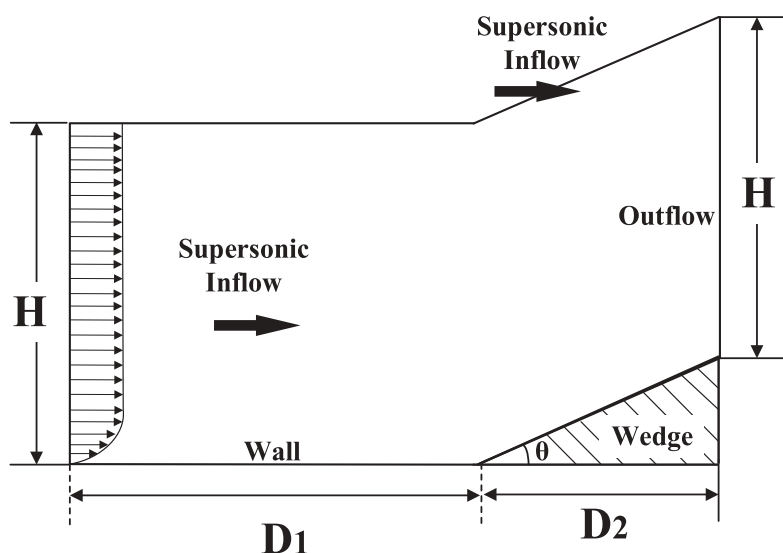


Figure 4. Schematic of the calculation domain and boundary conditions.

Numerical method

The two-dimensional simulations are conducted based on multi-species Navier-stokes equations, the governing equations are as follows,

$$\frac{\partial \rho}{\partial t} + \nabla \cdot (\rho \mathbf{U}) = 0 \quad (1)$$

$$\frac{\partial}{\partial t}(\rho \mathbf{U}) + \nabla \cdot (\rho \mathbf{U} \mathbf{U}) + \nabla p - \nabla \cdot \hat{\boldsymbol{\tau}} = 0 \quad (2)$$

$$\frac{\partial}{\partial t}(\rho Y_i) + \nabla \cdot (\rho Y_i \mathbf{U}) + \nabla \cdot \mathbf{J}_i - \dot{\omega}_i = 0 \quad (3)$$

$$\frac{\partial}{\partial t}(\rho E) + \nabla \cdot (\mathbf{U}(\rho E + p)) - \nabla \cdot \left(k_{eff} \nabla T - \sum_i h_i \mathbf{J}_i + \hat{\boldsymbol{\tau}} \cdot \mathbf{U} \right) + S_h = 0 \quad (4)$$

where ρ is the density of the mixture, \mathbf{U} is the velocity, E is the total energy, p is the pressure. Y_i and $\dot{\omega}_i$ are the mass fraction and the mass production rate of species i , respectively. S_h is the heat release of chemical reaction, k_{eff} is the effective thermal conductivity ($k_{eff} = k + k_t$, where k_t is the turbulent thermal conductivity).

The stress tensor $\hat{\boldsymbol{\tau}}$ is calculated with:

$$\hat{\boldsymbol{\tau}} = \mu \left[(\nabla \mathbf{U} + \nabla \mathbf{U}^T) - \frac{2}{3} \nabla \cdot \mathbf{U} \mathbf{I} \right] \quad (5)$$

where $\mu = \mu_l + \mu_t$ (μ_l is the laminar viscosity coefficient, and μ_t is the turbulent viscosity coefficient) is the molecular viscosity coefficient. \mathbf{I} is the unit tensor.

\mathbf{J}_i is the diffusion flux of species i generated by gradients of concentration and temperature. In turbulence flows, the mass diffusion is calculated with:

$$\mathbf{J}_i = - \left(\rho D_{i,m} + \frac{\mu_t}{Sc_t} \right) \nabla Y_i - D_{T,i} \frac{\nabla T}{T} \quad (6)$$

where $D_{i,m}$ and $D_{T,i}$ are the mass diffusion coefficient and the thermal diffusion coefficient for species i , respectively; Sc_t is the turbulent Schmidt number.

The total energy E is calculated with:

$$E = \sum_{i=1}^K Y_i h_i + \frac{1}{2} (u^2 + v^2) - \frac{p}{\rho} \quad (7)$$

where h_i is the enthalpy of species i , which is written as:

$$h_i = h_f^0 + \int_{T_{ref}}^T C_{pi} dT \quad (8)$$

where C_{pi} is the specific heat at constant pressure, h_f^0 is the formation enthalpy. C_{pi} is treated as a function of the temperature, and is calculated with a fitting function, expressed as:

$$c_{pi}(T) = a_{1,i} + a_{2,i}T + a_{3,i}T^2 + a_{4,i}T^3 + a_{5,i}T^4, \quad i = 1, \dots, K \quad (9)$$

The parameters in equation (9) can be consulted in the JANAF table (Stull and Prophet, 1971). The state equation is employed:

$$p = RT \sum_{i=1}^K \frac{\rho_i}{W_i} \quad (10)$$

where R is the universal gas constant.

In the simulations, a second-order MUSCL-TVD finite volume method is adopted for convection flux discretization, a hybrid Roe-HLL Riemann solver is used.

Reynolds averaging method is used in the present paper, the solution variables in the instantaneous Navier-Stokes equations are decomposed into the mean (ensemble-averaged) and fluctuating components. After decomposing, the final form of the Navier-Stokes equations is the same as the original except the new turbulence terms, $-\rho \overline{u'_i u'_j}$, which is called Reynolds stresses. To model Reynolds stresses and close the RANS equations, the Boussinesq hypothesis is employed to relate the Reynolds stresses to the mean velocity gradients.

$$-\rho \overline{u'_i u'_j} = \mu_t \left(\frac{\partial u_i}{\partial x_j} + \frac{\partial u_j}{\partial x_i} \right) - \frac{2}{3} \left(\rho k + \mu_t \frac{\partial u_k}{\partial x_k} \right) \delta_{ij} \quad (11)$$

The laminar viscosity coefficient, μ_p , is calculated by Sutherland's law, and the turbulent viscosity coefficient, μ_t , is obtained from Spalart-Allmaras turbulence model (Spalart and Allmaras 1992), which is presented as:

$$\frac{\partial}{\partial t}(\rho \tilde{v}) + \frac{\partial}{\partial x_i}(\rho \tilde{v} u_i) = G_v + \frac{1}{\sigma_{\tilde{v}}} \left[\frac{\partial}{\partial x_j}(\mu + \rho \tilde{v}) \frac{\partial \tilde{v}}{\partial x_j} \right] + C_{b2} \rho \left(\frac{\partial \tilde{v}}{\partial x_j} \right) - Y_v \quad (12)$$

where G_v and Y_v are the production and the destruction of turbulent viscosity, respectively. $\sigma_{\tilde{v}}$ and C_{b2} are the constants. The transport variable, \tilde{v} , can be used to compute the turbulent viscosity, μ_t , that is:

$$\mu_t = \rho \tilde{v} \frac{\left(\frac{\tilde{v}}{\nu} \right)^3}{\left(\frac{\tilde{v}}{\nu} \right)^3 + C_{v1}} \quad (13)$$

where ν is the molecular kinematic viscosity and C_{v1} is a constant. More details about the calculation method of each term and model constants can be consulted in Ref. (Spalart and Allmaras 1992).

Chemical interactions are modeled by a kinetic mechanism incorporating 9 gaseous species and 19 reversible reactions between them (Browne, Ziegler, Shepherd 2004). The mechanism is shown in Table 1. The inflow conditions of cases in the present paper are shown in Table 2.

The reaction rate of each reaction is modeled using the Arrhenius law:

Table 1. Chemical kinetic mechanisms components: O₂, H₂O, H, O, OH, H₂, H, O₂, H₂O₂, N₂.

	Reaction	A_r (mol-cm-s-K)	n_r	T_{ar} (K)
1	H ₂ + O ₂ = HO ₂ + H	1.00E+14	0	56034.7
2	H+ O ₂ = OH+O	2.60E+14	0	16810.4
3	H ₂ + O = OH+H	1.80E+10	1	8905.5
4	H ₂ + OH = H+ H ₂ O	2.20E+13	0	5153.2
5	OH+OH = O+ H ₂ O	6.30E+12	0	1090.7
6	H+ OH+M = H ₂ O+M	2.20E+22	-2	0
H ₂ O = 6.0				
7	H + H + M = H ₂ + M	6.40E+17	-1	0
H ₂ = 2.0; H ₂ O = 6.0				
8	H + O + M = OH+M	6.00E+16	-0.6	0
H ₂ O = 5.0				
9	H+ O ₂ + M = HO ₂ + M	2.10E+15	0	-1000.6
H ₂ = 2.0; H ₂ O = 16.0				
10	O + O + M = O ₂ + M	6.00E+13	0	-1801.1
11	HO ₂ + H = OH+OH	1.40E+14	0	1080.7
12	HO ₂ + H = H ₂ O+O	1.00E+13	0	1080.7
13	HO ₂ + O = O ₂ + OH	1.50E+13	0	950.6
14	HO ₂ + OH = H ₂ O+O ₂	8.00E+12	0	0
15	HO ₂ + HO ₂ = H ₂ O ₂ + O ₂	2.00E+12	0	0
16	H+ H ₂ O ₂ = H ₂ + HO ₂	1.40E+12	0	3602.2
17	O+ H ₂ O ₂ = OH+HO ₂	1.40E+13	0	6404
18	OH+H ₂ O ₂ = H ₂ O+HO ₂	6.10E+12	0	1430.9
19	H ₂ O ₂ + M = OH+OH+M	1.20E+17	0	45528.2
H ₂ O = 15.0				

Table 2. Inflow conditions of the cases in the present paper.

Case	T_0 (K)	P_0 (kPa)	M_0	ER	θ
1	872	63	3.6	0.34	22°
2	872	63	2.9	0.2	22°
3	872	63	2.9	0.25	22°
4	872	63	2.9	0.3	22°
5	872	63	2.9	0.35	22°
6	872	63	3.0	0.35	22°

$$k_{fr} = A_r T^{n_r} \exp\left(-\frac{T_{ar}}{T}\right) \tag{14}$$

Reverse reaction rates are obtained using the minimal Gibbs energy principle:

$$k_{b,r}(T) = \frac{k_{f,r}(T)}{K_r(T)} \tag{15}$$

$$K_r(T) = \exp\left(\frac{\sum_{i=1}^N \left(v''_{i,r} - v'_{i,r}\right) G_i^0(T)}{RT}\right) \left(\frac{P_{atm}}{RT}\right)^{\sum_{i=1}^N \left(v''_{i,r} - v'_{i,r}\right)} \tag{16}$$

where P_{atm} is the standard atmosphere pressure, G_i^0 is a molar Gibbs energy of component i at the atmosphere pressure. $v'_{i,r}$ and $v''_{i,r}$ are the input and output stoichiometric coefficients of species i in reaction r , respectively.

Therefore, the generation rate of species i , $\dot{\omega}_i$ is expressed as:

$$\dot{\omega}_i = W_i \sum_r (v''_{i,r} - v'_{i,r}) \left(k_{f,r}(T) \prod_{j=1}^N \left(\frac{\rho Y_j}{W_j} \right)^{\eta'_{j,r}} - k_{b,r}(T) \prod_{j=1}^N \left(\frac{\rho Y_j}{W_j} \right)^{\eta''_{j,r}} \right) \quad (17)$$

Validation of numerical method

For the lack of experimental investigations including both boundary layer separation and ODW, the validation of the numerical method is conducted similar to Ref. (Liu, Zhou, Lin 2015), where the experiment on SBLI problem conducted by Dolling and Murphy (Dolling and Murphy 1983) was chosen. In their experiments, the incoming Mach number is 2.9, the total pressure is 680 kPa, the stagnation temperature is 265 K, and the thickness of the incoming boundary layer is 2.2 cm with a Reynolds number of 7.8×10^5 . The ramp angle is 24° , and the length and the width of the ramp surface are both 15 cm. Numerical simulation under the same condition is carried out and the comparison of the shadowgraphs and wall pressure distributions between the experimental and numerical results are shown in Figures 5 and 6.

It is shown that the numerical shadowgraph and wall pressure distributions are consistent with the experimental results very well, which proves the reliability of the numerical method in simulating flowfields involving large-scale separation caused by SBLIs.

Results and discussion

In an ODW with an abrupt transition, the existence of the primary triple point and the primary transverse wave makes the ODW structure more complicated. Because of the huge difference in structures between the two kinds of transitions, they should be

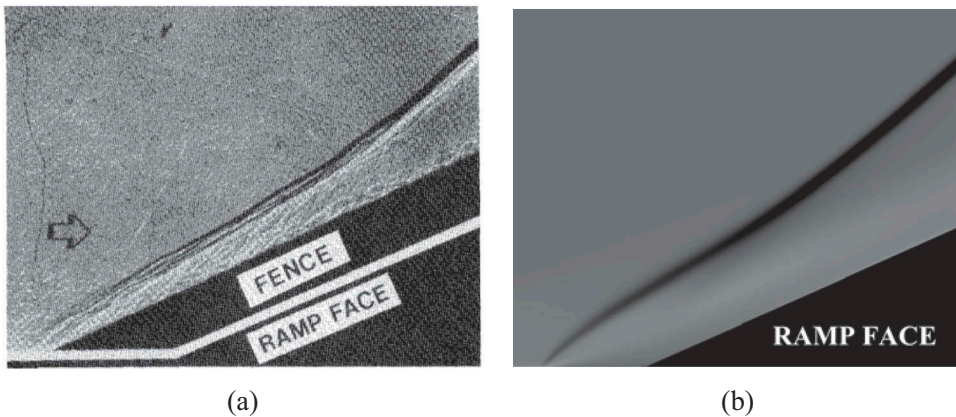


Figure 5. Comparison of shadowgraphs between experimental and numerical results. (a) Shadowgraph of experimental results. (b) Shadowgraph of numerical results.

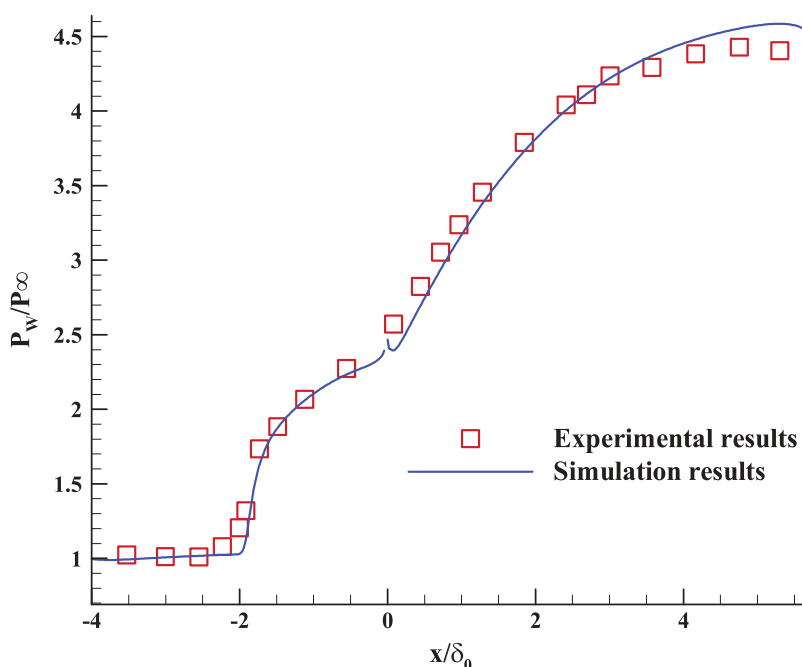


Figure 6. Comparison of wall pressure distributions between experimental and numerical results.

studied separately. In this paper, several typical cases are simulated, which are listed in Table 1.

SBLI in ODWs with smooth transitions

Firstly, SBLIs in ODWs with smooth transitions and their influence on the characteristics of ODWs are investigated. The inflow condition is chosen as $T_0 = 872$ K, $P_0 = 63$ kPa, $M_0 = 3.6$, $ER = 0.34$ and $\theta = 22^\circ$, under which a smooth transition occurs. To make a comparison, three different cases are simulated, and the flowfields at the time of $370 \mu\text{s}$ are all shown in Figure 7. Figure 7(a) gives the ODW structure in an inviscid flow. Figure 7(b) shows the ODW structure in a viscous flow without inflow boundary layer (IBL), where the lower wall of the parallel channel is set to be symmetric boundary. Figure 7(c) shows the ODW structure in a viscous flow with IBL, where the lower wall of the parallel channel is set to be no-slip adiabatic wall.

It is shown that smooth transitions are achieved in inviscid and viscous flows, and the overall structures are similar. The induced shock wave transits to the ODW smoothly without any triple points and transverse waves. When the IBL is not considered, which is shown in Figure 7(b), the ODW structure in viscous flow is almost the same as that in inviscid flow. That means, the post-wave boundary layer has little effects on the overall structure, which is consistent with previous studies (Li, Kailasanath, Oran 1993b). Actually, for an ODW with a smooth transition, there are no primary transverse waves. That means, there are no shock waves interacting with the post-wave boundary layer. Without SBLI phenomena, the overall structure of ODW changes little, which is consistent with previous results (Li, Kailasanath, Oran 1993b). The structure can be depicted by Figure 8.

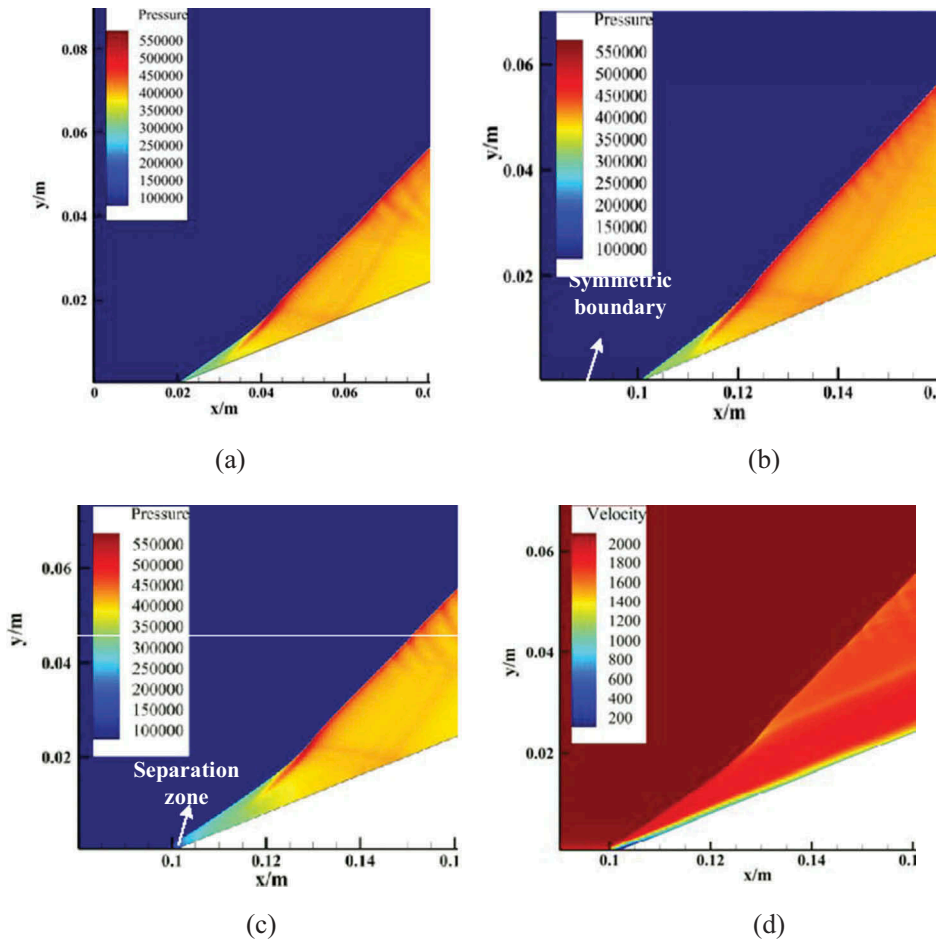


Figure 7. ODW structures in inviscid and viscous flows. (a) ODW in inviscid flow. (b) ODW in viscous flow without IBL. (c) Pressure contour of ODW in viscous flow with IBL. (d) Velocity contour of ODW in viscous flow with IBL.

However, when the IBL is considered, which is shown in Figure 7(c), SBLI occurs and a ramp-induced separation is formed compared with Figure 7(b). Under the circumstances, the transition area between the oblique shock and the oblique detonation moves downstream slightly. To make it clear, the wall and the wave pressure distributions are extracted, which are shown in Figure 9.

From Figure 9(a), the ramp-induced separation is relatively small, but it still affects the ODW flowfield obviously. Compared with the inviscid flow, the wall pressure affected by IBL increases gradually, and an additional distance of 0.01 m is needed for the pressure to increase to the same value as the inviscid flow.

According to the definition in Ref. (Yang et al. 2018; Yu and Miao 2018), the projected length of the induced shock wave along the x -axis is defined as the initiation length, which is also the distance between the pressure peak and the wedge tip in Figure 9(b). From Figure 9(b), the initiation length in inviscid flow is about 0.0230 m while that of viscous

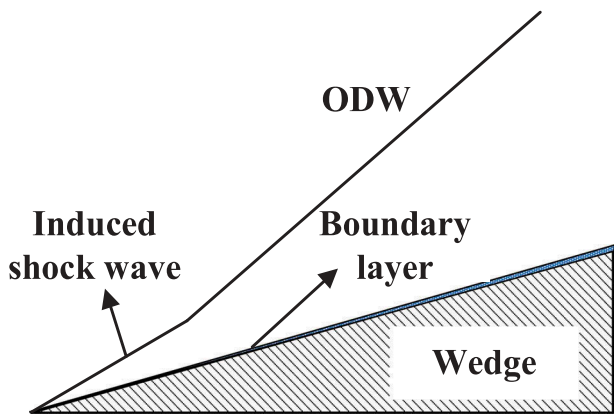


Figure 8. Sketch of ODWs with smooth transitions affected by post wave boundary layer (PWBL).

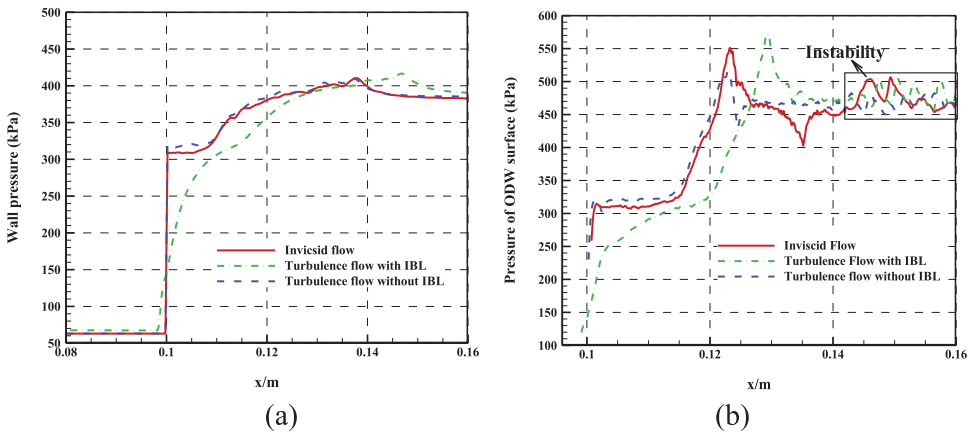


Figure 9. Wall and wave pressure distributions under different conditions. (a) Wall pressure curves. (b) Wave pressure distributions.

flow without IBL is 0.0228, which are nearly the same. In contrast, the initiation length affected by IBL, which is shown in Figure 9(c), is about 0.029 m with an increase of 26% compared with that of inviscid flow. That means, the change of initiation length is not decided by the numerical method but related to the effects of IBL. Because the chemical reaction does not occur at the tip of the wedge, the interaction between inert shock and boundary layer is responsible for the ramp-induced separation. Figure 10 gives the sketch of the ramp-induced SBLI with separation, and the reason why the initiation length changes can be explained.

In the ramp-induced SBLI, when the strength of the wedge-induced shock exceeds the capacity of the boundary layer to withstand the compression, separation occurs at point S located upstream of the ramp apex, which is shown in Figure 10. Then separation shock (C1) is formed due to the focusing of the compression waves induced by the separation process. Downstream of S, the fluid in the boundary layer near the wall recirculates,

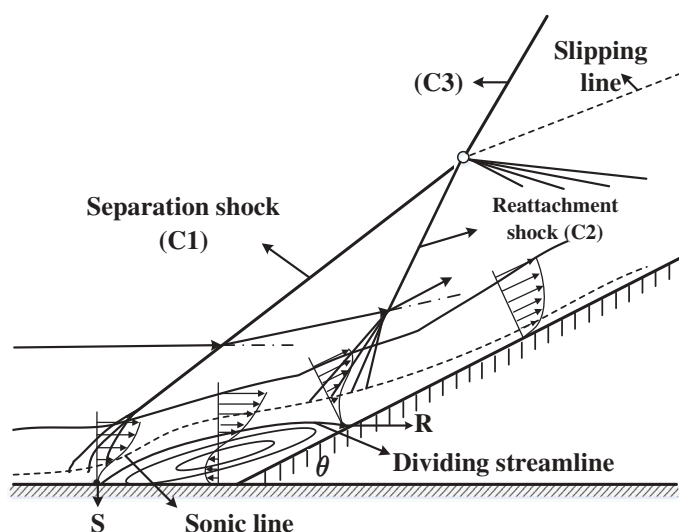


Figure 10. Sketch of the flow induced by a ramp with separation.

leading to the formation of the separation bubble. Reattachment at R on the wedge surface gives rise to the reattachment shock (C2). Then, C1 and C2 focus at point T, and the focused shock (C3) is formed. Li et al. (Li, Kailasanath, Oran 1993b) indicated that in an ODW flowfield, the combustion generated by thermal dissipation is confined to the boundary layer and does not ignite the mixture in the flow outside of the boundary layer. That means the chemical reactions in the boundary layer can not initiate the ODW. Actually, the initiation of ODW depends on the compression effects of the wedge-induced shock, and only when the compression effects make the concentration of the free radicals high enough, there are enough energy released for the initiation of ODWs. It is shown in Figure 9(b) that the wave pressure is just about 200 kPa near the separation zone, which indicates that the separation shock (C1) is too weak to initiate the mixture. So the compression effects of the focused shock (C3) is the main cause of the initiation of ODW. When affected by IBL, the focused shock moves downstream, which delays the compression effects, leading to the increase of initiation length of ODW.

SBLI in ODWs with abrupt transitions

ODWs with abrupt transitions are more complicated, where the primary transverse waves reflect on the wedge surface behind the ODW, so the SBLI problems are not as simple as that in smooth transitions. Therefore, special investigations are conducted in the following.

ODW structure with SBLI

The inflow condition is chosen as $P_0 = 63$ kPa, $T_0 = 872$ K, $ER = 0.34$, $M_0 = 2.9$ and $\theta = 22^\circ$, under which an abrupt transition appears. The velocity contour is shown in Figure 11.

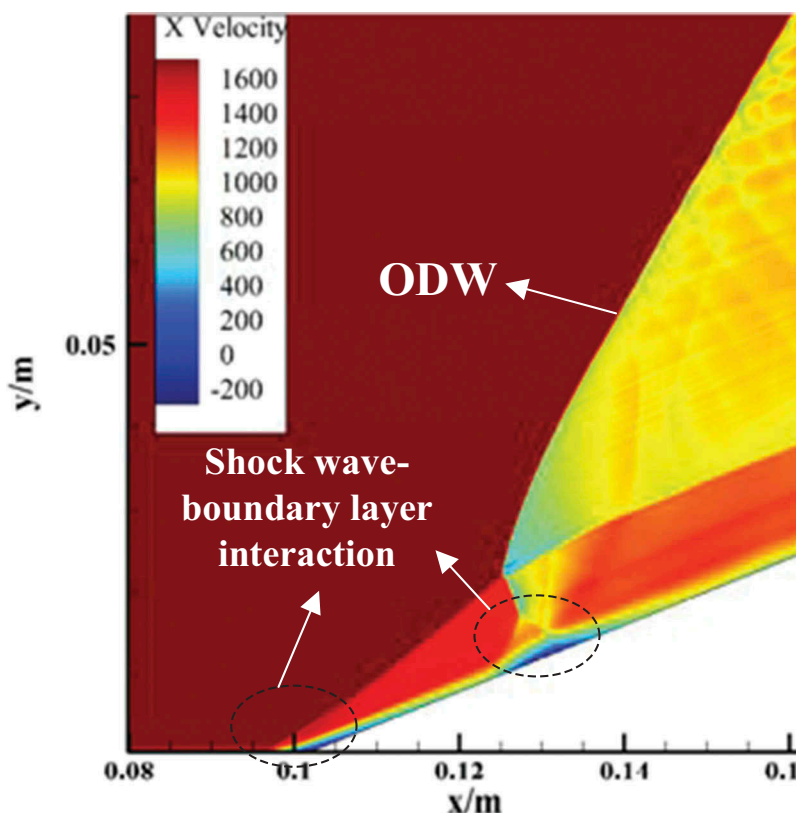


Figure 11. Velocity contour of ODW flowfield with SBLIs.

It is shown in [Figure 11](#) that there are two kinds of SBLI phenomena, i.e., SBLI induced by the ramp and SBLI induced by the primary transverse wave. The former is similar to the SBLI in ODWs with smooth transitions, where a separation zone is formed, leading to the upstream propagation of the induced shock. The wall pressure distributions and the wave pressure are shown in [Figure 12](#). As a comparison, the wall and wave pressure distributions of inviscid flow and viscous flow without IBL are also given.

It is shown that abrupt pressure rises appear in the wall and wave pressure curves. Apparently, the pressure peaks of wall pressure curves represent the positions where the primary transverse waves reflect on the wedge surface, while the pressure peaks of wave pressure curves are the primary triple points, which only appear in ODWs with abrupt transitions. Similar to the ODW with a smooth transition, the initiation length increases obviously due to the separation of the IBL. The mechanisms are also the same as that of ODWs with smooth transitions.

In the following, the second kind of SBLI, i.e. the post-wave SBLI induced by the primary transverse wave, is focused on. As is shown in [Figure 11](#), the primary transverse wave originates from the primary triple point and reflects on the wedge surface. The incident transverse wave interacts with the post-wave boundary layer, leading to the occurrence of the second kind of SBLI. Therefore, the primary transverse wave is the dominant cause of the post-wave SBLI and that is why it is not formed in ODWs with

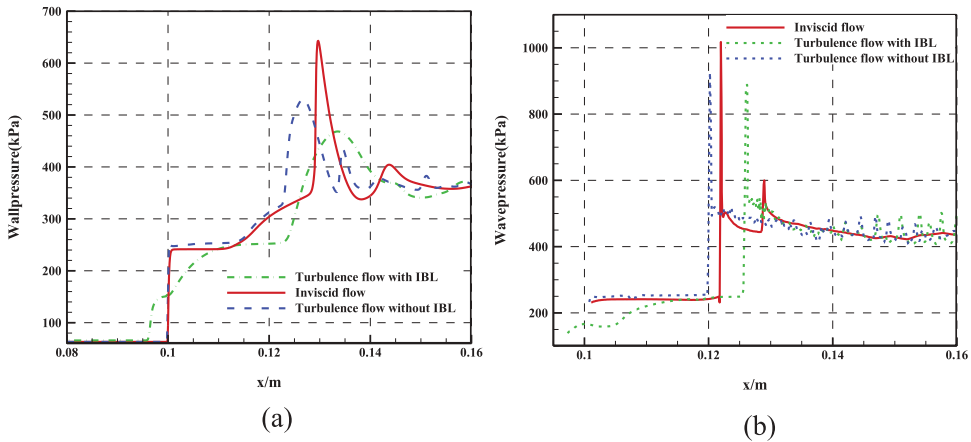


Figure 12. Wall and wave pressure distributions of ODW flowfield. (a) Wall pressure distributions. (b) Wave pressure distributions.

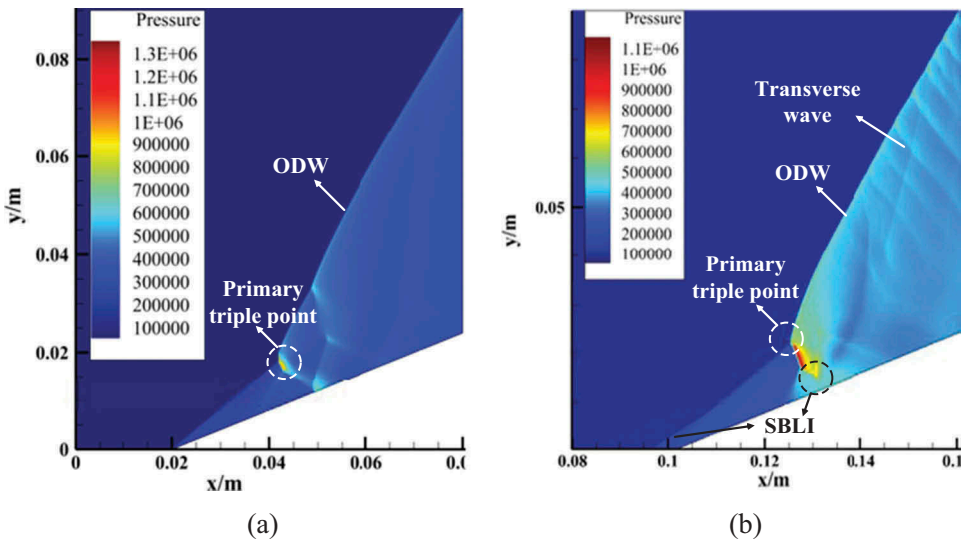


Figure 13. Comparison between ODW structures with and without SBLIs. (a) Pressure contour of ODW in inviscid flow. (b) Pressure contour of ODW affected by SBLIs.

smooth transitions. The pressure contour of ODWs in inviscid and viscous flows are shown in Figure 13.

It is indicated that abrupt transitions are formed both in inviscid and viscous flows under the given condition, where the primary triple points and the primary transverse waves are depicted. However, the reflection structures in Figure 13(a) and (b) are quite different. In the inviscid flow, a regular reflection occurs while a Mach stem appears in the viscous flow due to the post-wave SBLI. Because the primary transverse wave is much weaker than the ramp-induced shock, the post-wave SBLI is a kind of weakly interacting flow, where there is only

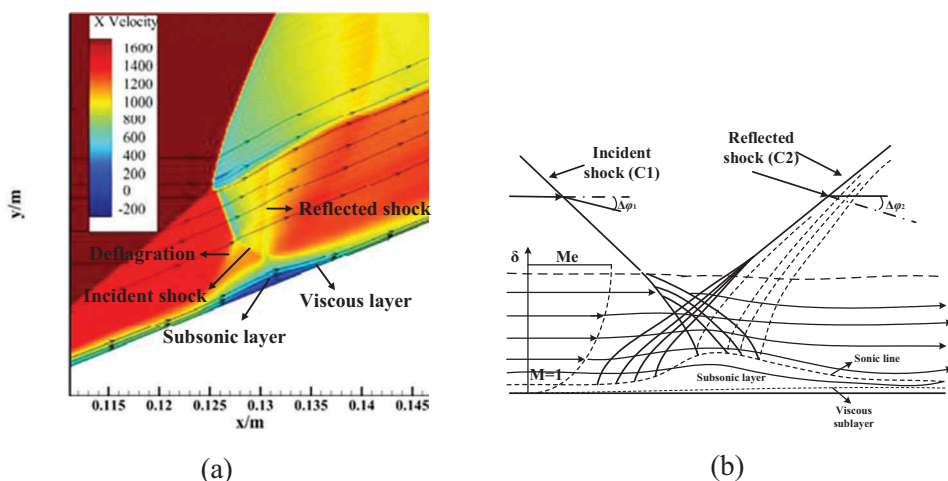


Figure 14. Flow structure of SBLI behind an ODW with an abrupt transition. (a) Flow structure of post-wave SBLI. (b) Sketch of a shock reflection without boundary layer separation.

subsonic layer formed instead of separation zone. The enlarged view of Figure 11 and the sketch of a shock reflection without boundary layer separation are shown in Figure 14.

Part of streamlines are given in Figure 14(a), which demonstrates the absence of separation zone in the weakly interacting flow. The primary transverse wave penetrates the rotating inviscid part of the boundary layer, where it progressively bends because of the decrease of the local Mach number. Correspondingly, the intensity weakens and vanishes altogether when it reaches the boundary-layer sonic line. Meanwhile, the pressure rise through the incident shock (C1) is experienced upstream of where C1 would have impacted the wall in the absence of a boundary layer. The pressure rise caused by the shock is transmitted upstream through the subsonic part of the boundary layer. This leads to a spreading of the wall-pressure distribution over a distance on the order of the boundary layer thickness, compared to the purely inviscid flow solution, which is shown in Figure 12(a). Besides, it is shown in Figure 14(a) that the incident angle of the transverse wave affected by the PWBL is larger than that of inviscid flow, which is almost vertical to the wedge surface. The OH-fraction contour is given in Figure 15.

According to Figure 15(a), except for the area next to the primary triple point, the transverse wave is isolated with the deflagration, indicating that the transverse wave is an inert shock. However, when affected by the post-wave SBLI, the primary transverse wave couples with combustion, leading to the formation of an overdriven detonation. Based on the previous study (Han 2013), when the transverse wave becomes a detonation and is vertical to the wedge surface, the ODW is critically stable, which is closer to the detachment state.

Effects of IBL thickness

According to the numerical results, two kinds of SBLIs coexist in ODWs with abrupt transitions for the complexity and the specificity of the flow structure. However, this phenomenon has never been reported in previous studies, and the reason is analyzed in the following.

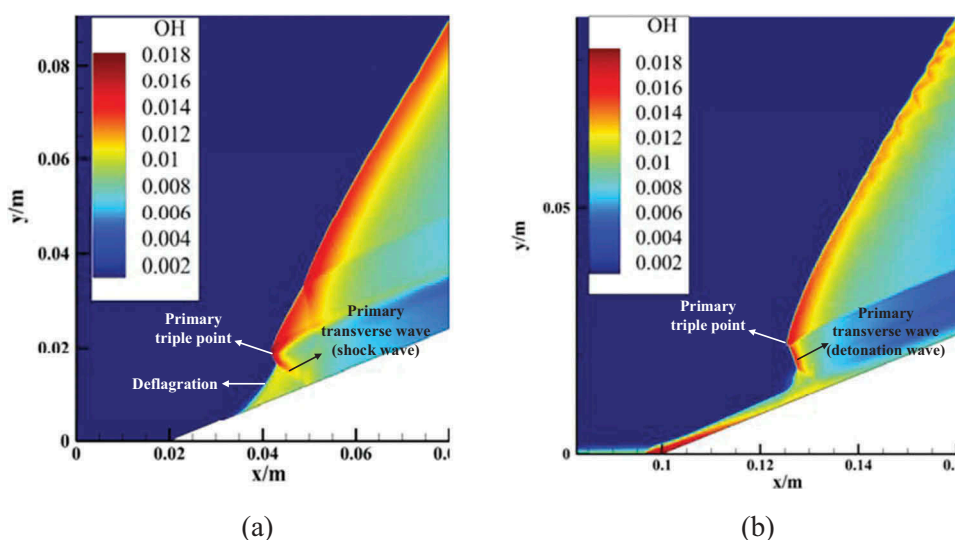


Figure 15. Contours of OH fractions of ODW flowfield. (a) Contour of OH fraction in inviscid flow. (b) Contour of OH fraction affected by SBLIs.

Li et al. (Li, Kailasanath, Oran 1993b) suggested that the overall structures of ODWs are not affected by PWBL, while the results in the present paper show a great influence of PWBL on the ODW flow structure. The reasons are as follows: (1) In the study of Li et al., numerical simulations are mainly focused on ODWs with smooth transitions. Based on the present results, there are no post-wave SBLIs in ODWs with smooth transitions due to the absence of the primary transverse wave, so the ODW structures are not affected by the PWBL obviously. (2) To save the calculation cost, a rectangular calculation domain was usually utilized in previous studies (Li, Kailasanath, Oran 1993b; Teng, Zhang, Jiang 2014), and IBLs can not be included in this kind of calculation domain. As discussed above, when IBL is not considered, the PWBL develops just from the wedge tip, which is too thin to affect the ODW structure.

Actually, the IBL can not be eliminated completely in a real engine, therefore, further investigations on the interactions between IBL and PWBL are conducted. The typical inflow condition is still employed in this section, that is, $P_0 = 63$ kPa, $T_0 = 872$ K, $ER = 0.34$, $M_0 = 2.9$, $\theta = 22^\circ$. The velocity contour of ODWs in viscous flows with and without IBL are shown in Figure 16.

It is shown that when there is no IBL, the PWBL starts from the wedge tip and is rather thin at the position where the transverse wave reflects, which is shown in Figure 16(a). Therefore, the post-wave SBLI is weak and the subsonic area is so small that the effects can be ignored. However, when the IBL exists, the thickness of PWBL increases apparently behind the ramp-induced separation, and when it reaches the position where the transverse wave reflects, a stronger post-wave SBLI occurs, leading to a larger subsonic area. Therefore, the PWBL, as well as the post-wave SBLI, is obviously promoted by the IBL, which in turn affects the ODW structure.

Actually, the thickness of IBL also plays an important role in the post-wave SBLI problem. To make a systematical analysis, different IBL thicknesses are selected, which

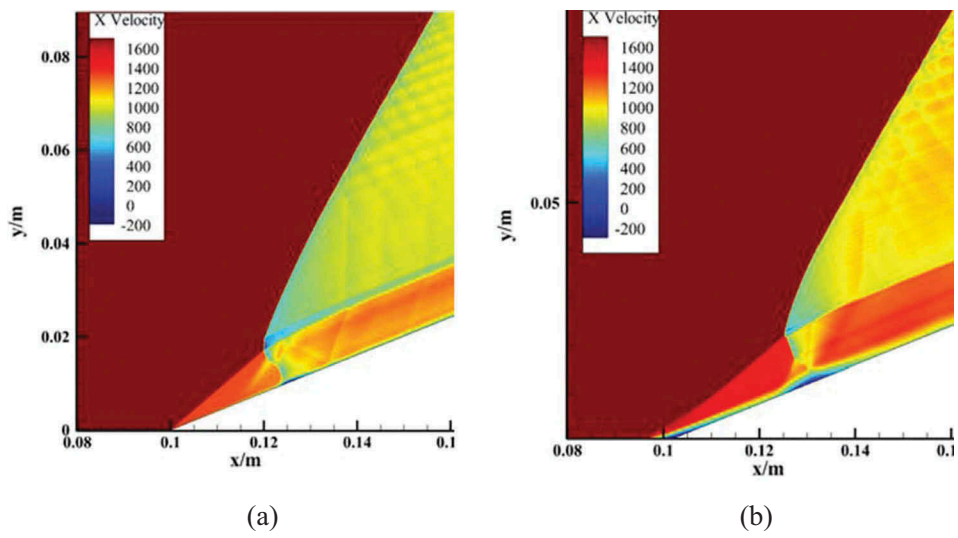


Figure 16. ODW structures affected by boundary layers. (a) ODW structure with PWBL, without IBL. (b) ODW structure with PWBL and IBL.

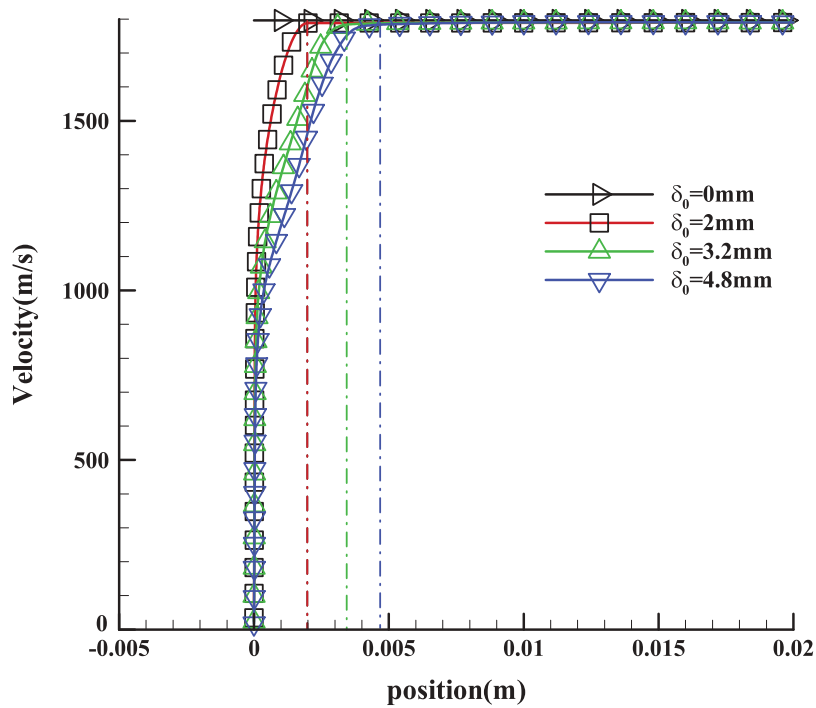


Figure 17. Velocity profiles along $x = 90\text{ mm}$.

are measured by the velocity profiles along $x = 90\text{ mm}$, locating at a distance of 10 mm from the wedge tip. The velocity profiles are shown in Figure 17.

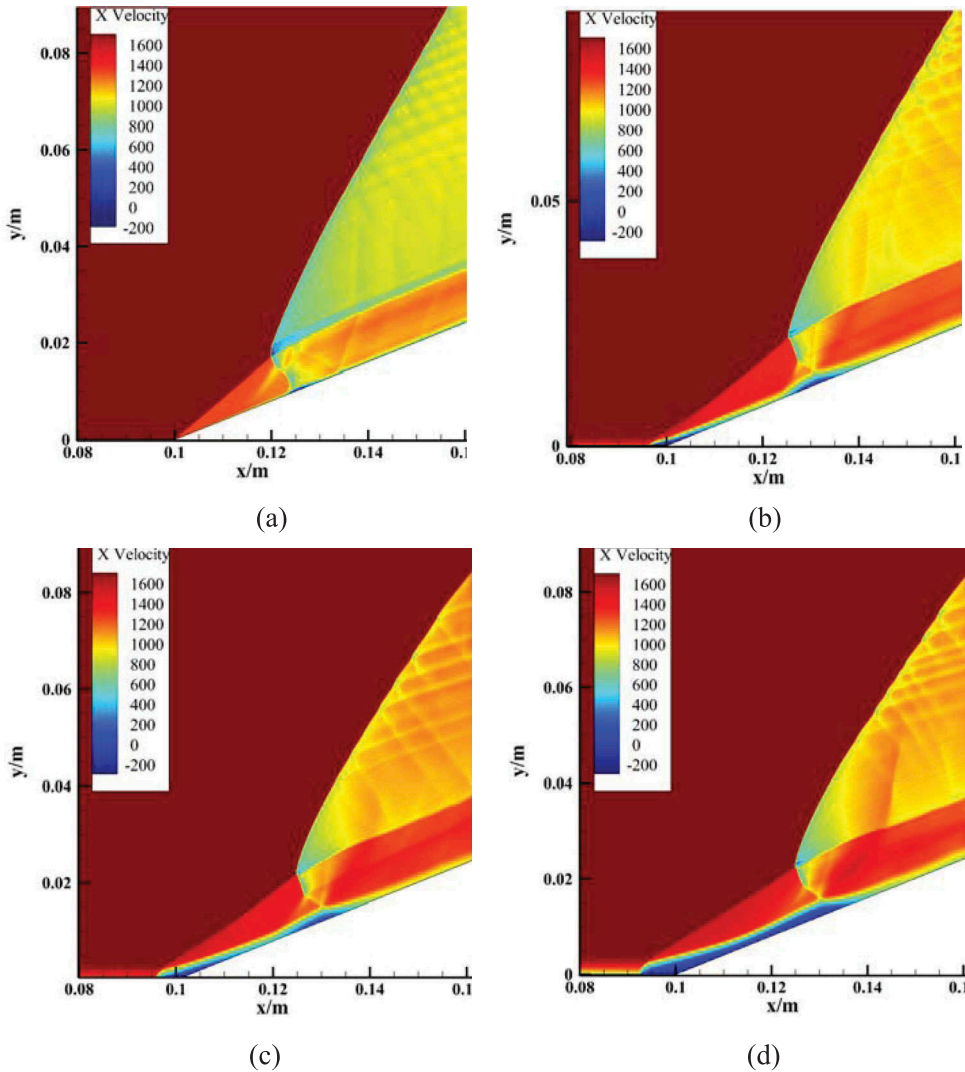


Figure 18. ODW structures with different IBL thicknesses. (a) $\delta_0 = 0$ mm. (b) $\delta_0 = 2$ mm. (c) $\delta_0 = 3.2$ mm. (d) $\delta_0 = 4.8$ mm.

From the velocity profiles, the thicknesses of the IBLs are 0 mm, 2 mm, 3.2 mm and 4.8 mm, respectively, and the corresponding velocity contours of ODW flowfields are shown in Figure 18.

It is shown in Figure 18(a) that when $\delta_0 = 0$ mm, the PWBL is thin and the post-wave SBLI is weak, where a negligible subsonic area is formed. When the boundary layer thickness increases to $\delta_0 = 2$ mm, a ramp-induced separation zone is formed, and the boundary layer thickness is kept at a comparative order at the reattachment position. Then the PWBL continues developing based on the IBL, leading to a remarkable increase in the thickness of PWBL, and the post-wave SBLI becomes stronger. In Figure 18(b), the ramp-induced separation zone and the post-wave subsonic area are separated, without interaction with each other. As the IBL thickness increases further, the ramp-induced separation and the post-wave subsonic area both become larger, and

the distance between them is shorter, which is shown in Figure 18(c). Until when the IBL becomes thick enough, i.e., $\delta_0 = 4.8$ mm in Figure 18(d), the ramp-induced separation and the post-wave subsonic area are so large that they merge together. Then the extended separation area covers on the whole induction zone behind the induced oblique shock, and affects the ODW structure more obviously. Figure 19 gives the schematic of the structural change of the ODW.

In summary, the two kinds of SBLIs, as well as the interaction between them, are affected by the thickness of IBL. When the IBL is thin, the ramp-induced separation and the post-wave subsonic area are both small, which are separated from each other. However, when the IBL is thick enough, the ramp-induced separation and the post-wave subsonic area both become larger and merge together, leading to an extended separation zone, which covers on the induction zone and affects the ODW structure more obviously.

Effects of abrupt degree

The size of the ramp-induced separation zone and the post-wave subsonic area are both affected by IBL, which dominates the SBLI problems in the ODW flowfields. According to traditional theories on SBLIs, the incident-reflecting flow is directly related with the strength of the incident shock. With regard to an ODW with an abrupt transition, the primary transverse wave acts as the incident shock in the post-wave SBLI, which represents the overall structure and the stability of the ODW. Therefore, special investigations are conducted on the effects of the strength of the primary transverse waves. Based on the previous study (Miao et al. 2018), the strength of the primary transverse wave is related to the reactivity of the inflow mixture. When the inflow velocity and the wedge angle are fixed, a higher reactivity represents a stronger primary transverse wave. Therefore, four cases with different equivalence ratios are chosen, while the inflow pressure, temperature, Mach number, wedge angle and IBL thickness are all kept unchanged. The ODW structures with different equivalence ratios are shown in Figure 20.

It is shown that with the increase of equivalence ratio, the post-wave subsonic area becomes lager, and finally merges with the ramp-induced separation. The main reasons are as follows: (1) with the increase of equivalence ratio, the primary transverse wave is stronger, leading to a stronger post-wave SBLI. So the subsonic area becomes larger, which

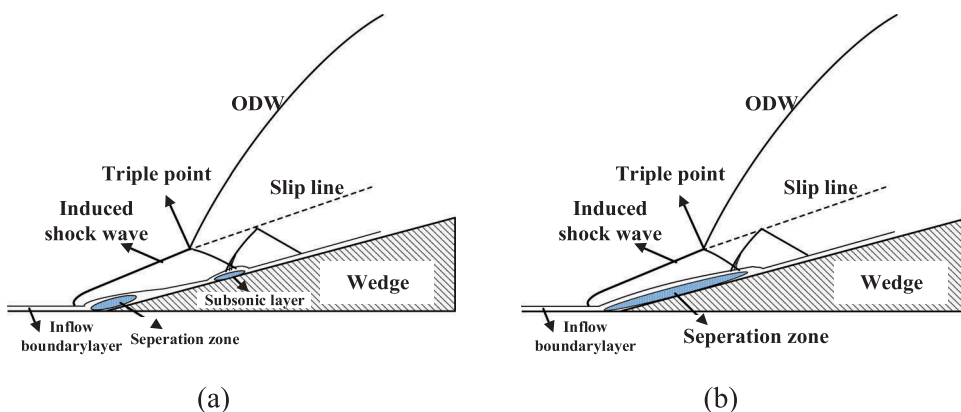


Figure 19. Schematic of ODW structure affected by SBLIs with different IBL thicknesses. (a) ODW structure with a thin IBL. (b) ODW structure with a thick IBL.

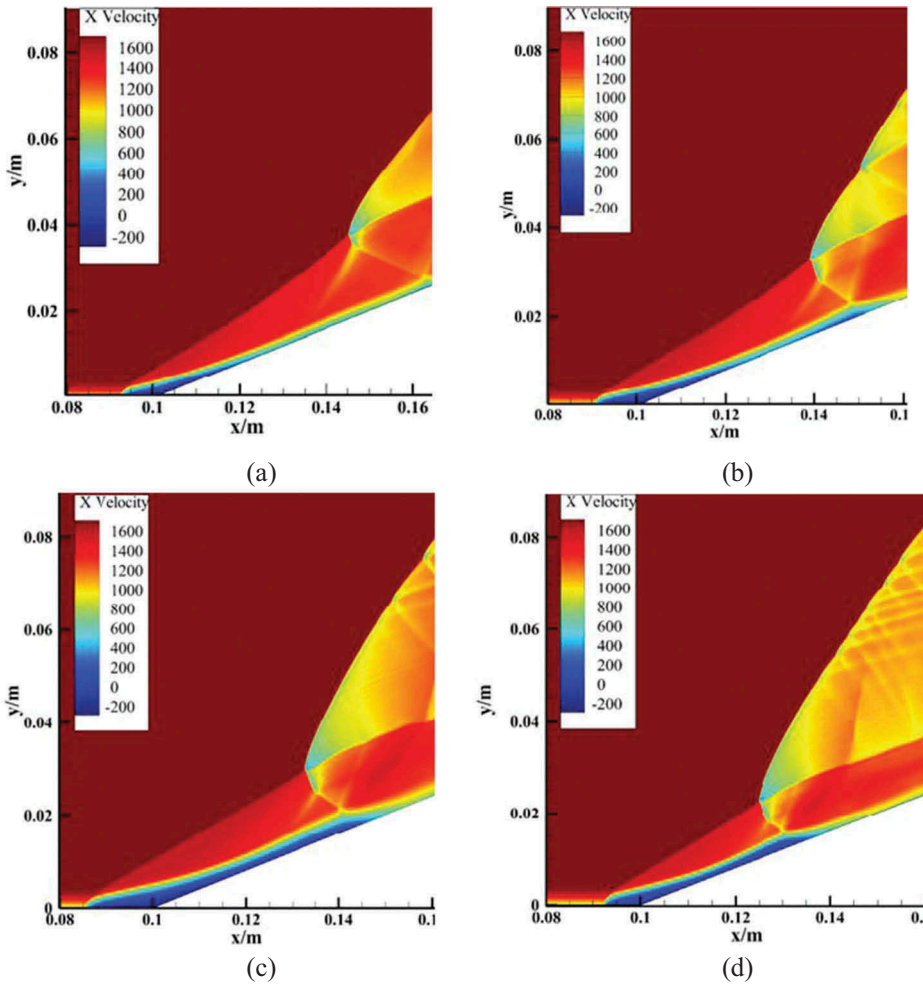


Figure 20. ODW structures with different equivalence ratios. (a) $ER = 0.2$. (b) $ER = 0.25$. (c) $ER = 0.3$. (d) $ER = 0.35$.

makes it easier to merge with the ramp-induced separation. (2) With the increase of the equivalence ratio, the activity of the premixed mixture is higher, leading to a shorter initiation length. That means, the post-wave subsonic area is closer to the ramp-induced separation, which also makes it easier for the two areas to merge together. Actually, once the ramp-induced separation merges with the post-wave subsonic area, the extended separation covers on the wedge surface in the induction zone, and it will affect the stability of the ODW obviously, which is to be discussed in the following section.

Discussion about the stability of ODW

According to the preceding results, the abrupt ODW structures affected by SBLIs can be divided into two kinds, i.e., the ramp-induced separation is separated from the post-wave subsonic area, and the ramp-induced separation merges with the post-wave subsonic area.

As is mentioned in the introduction part, Teng et al. (Teng, Zhang, Jiang 2014) observed three kinds of shock configurations, i.e., the λ -shaped shock, the X-shaped shock, and the Y-shaped shock, at the end of the induction zone. Their results showed that the X-shaped and Y-shaped shocks appear when the incident Mach number is low, and the Y-shaped shock is associated with the complicated unstationary process. Besides, the induction zone is dominated by the oblique shock in the λ -shaped shock configuration while it is dominated by the oblique detonation in the Y-shaped shock configuration. Actually, in the studies of Teng et al., the shock configuration changes from the λ -shaped to the Y-shaped shock when the incident Mach number decreases from $M_0 = 7$ to $M_0 = 6.7$. As we know, ODWs can only be stabilized under proper conditions. When the incident Mach number decreases while other conditions are kept unchanged, the ODW will be closer to the detachment state.

Therefore, ODWs with Y-shaped shocks are less stable than ODWs with λ -shaped shocks. According to the simulation results under the typical condition, the λ -shaped and Y-shaped shocks are formed in inviscid flow and in the boundary layer affected flow, respectively. The flow structures are shown in Figure 21(a) and (b), indicating that the post-wave SBLI weakens the stability of ODWs.

Besides, Figure 15 shows that the primary transverse wave affected by the PWBL changes from an inert shock to an overdriven detonation, which is vertical to the wedge surface. Actually, similar shock configurations were also observed in the study of Han et al. (Han 2013) in inviscid flows under the critical condition. In the present paper, a critical condition, i.e., $P_0 = 63\text{kPa}$, $T_0 = 872\text{K}$, $ER = 0.35$, $M_0 = 3.0$, $\theta = 22^\circ$, is also selected and the corresponding ODW flowfield is simulated. Figure 22 gives the ODW structure under the critical condition.

It is demonstrated that the shock configuration where the primary transverse wave is vertical to the wedge surface only occurs under the critical condition, which is close to the

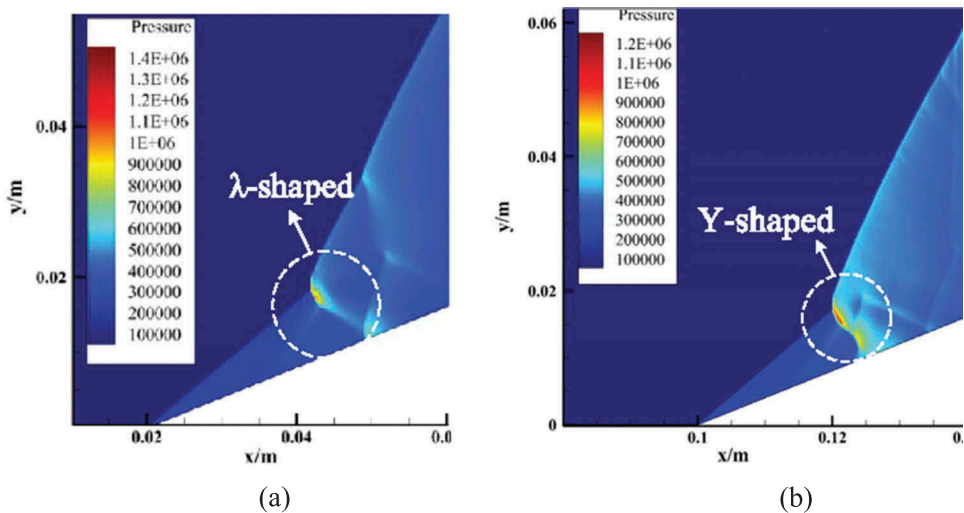


Figure 21. Shock configurations under different conditions. (a) λ -shaped shock configuration in inviscid flow. (b) Y-shaped shock configuration affected by the PWBL.

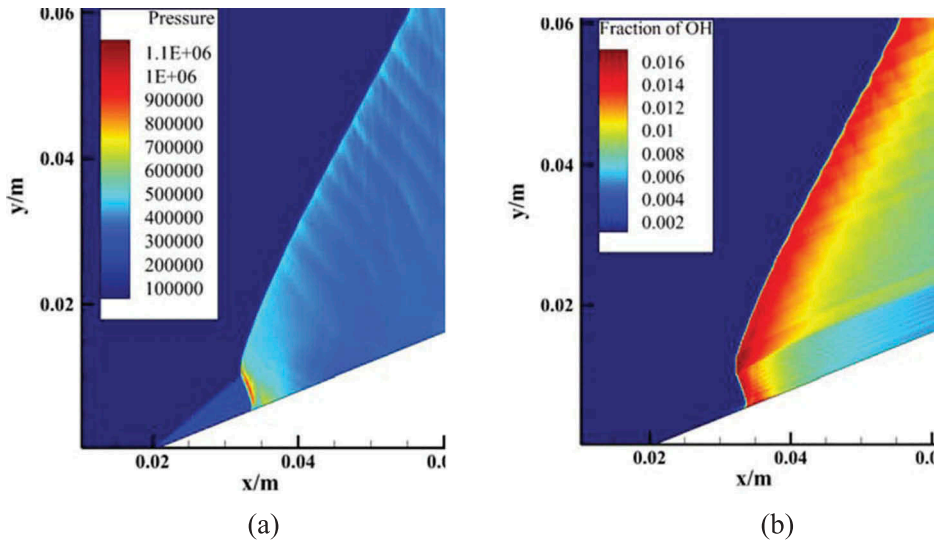


Figure 22. ODW flow structure under critical condition. (a) Pressure contour of ODW. (b) Contour of OH fraction.

detachment state. The similarity between [Figures 15\(b\)](#) and [22\(b\)](#) verifies the instability of the ODW affected by the post-wave SBLI.

In conclusion, when the ramp-induced separation is separated from the post-wave subsonic area, the shock configuration changes and the stability of ODW is weakened, but the ODW is still stabilized on the wedge surface. However, when the ramp-induced separation merges with the post-wave subsonic area, it differs a lot, especially under the critical condition. To make a comparison, the ODW under the critical condition and affected by SBLIs is simulated. The shadowgraph and the velocity contour are shown in [Figure 23](#).

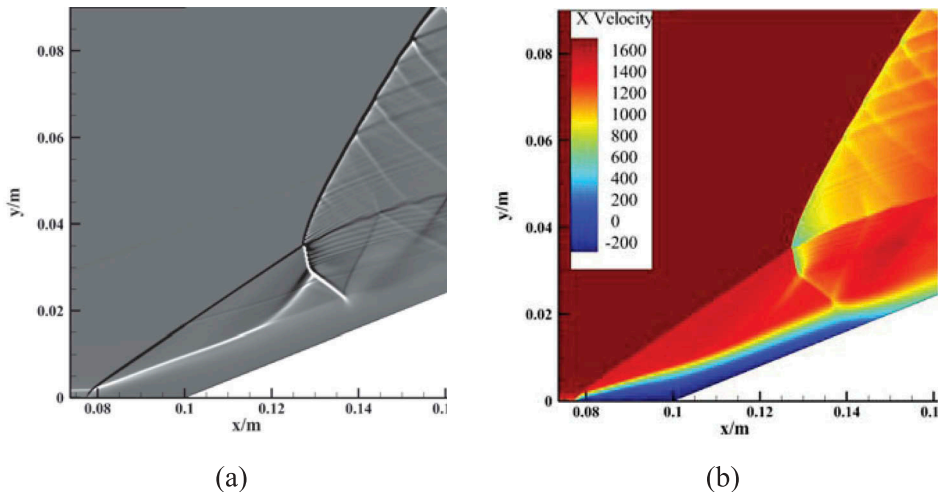


Figure 23. ODW flowfields affected by SBLIs under the critical condition. (a) Shadowgraph of ODW flowfield. (b) Velocity contour of ODW flowfield.

It is indicated that the ramp-induced separation and the post-wave subsonic area merge together under the critical condition. The extended separation covers on the wedge surface in the induction zone. Under the circumstances, the separation zone acts as a gasdynamic wedge whose angle is smaller than the physical wedge, leading to a great change in ODW structure. According to Figure 22, the angle of the ODW in inviscid flow is about 63.3° . As a comparison, the ODW angle affected by SBLIs is about 58.6° , which is obviously smaller than that of the inviscid flow. Provided the gasdynamic wedge angle is treated as the actual wedge angle, i.e. $\theta = 20^\circ$, the ODW angle should be 59.8° theoretically, which is closer to the simulation result in Figure 23.

However, as the calculation time increases, this kind of ODW structure can not keep stable all the time. Actually, when the post-wave subsonic area merges with the ramp-induced separation, the pressure rise through the primary transverse wave propagates upstream to the front of the separation zone, leading to an upstream propagation of the separation point. In other words, the separation is extended. As the separation expands, the initiation length of ODW increases, and the ODW propagates downstream towards the outlet of the channel. As the pressure rise and the separation expansion interact with each other, further expansion is promoted. Finally, the size of the separation zone is comparable with and even larger than the wedge length, which makes the ODW propagate out of the calculation domain and fail to be stabilized on the wedge.

According to the present results, the structure and stability of wedge-induced ODWs are detrimentally affected by boundary layers, so the SBLI problems should be avoided in a real engine. From this point of view, ODWs with smooth transitions are preferred in a real ODWE, where SBLI problems are weaker for the simple wave structures.

However, the Reynolds averaging method is utilized in the present paper and the turbulence intensity is set to a very small value, so the vicious flows are still laminar flows, where the turbulent effects are not considered. SBLIs in ODWs affected by strong turbulence effects need further specific investigations.

Conclusions

In the present paper, numerical investigations on ODWs affected by boundary layers are conducted. SBLI problems in ODWs with smooth and abrupt transitions are investigated separately. The results show that there are no shock waves behind detonation wave surface for ODWs with smooth transitions, so the flow structures are only affected by the ramp-induced SBLI. Under the influence of IBL, the compression effects of the focused shock instead of the separation shock is the main cause of the initiation of ODW, which leads to an obvious increase in the initiation length. With regard to ODWs with an abrupt transition, the flow structure is affected by two kinds of SBLI problems, i.e., the ramp-induced SBLI and the SBLI induced by the primary transverse wave. The former one forms with a ramp-induced separation while the latter one occurs with a subsonic area instead of any separations. The effects of IBL is similar to that of ODWs with smooth transitions, where the initiation length increases. Besides, the SBLIs are affected by the thickness of the inflow boundary layer and the equivalence ratio. When the IBL is thin and the equivalence ratio is low, the separation zone is small and the distance between the ramp-induced separation zone and the post-wave separation zone is large, which makes the ramp-induced separation separated from the post-wave subsonic area. Under the circumstances, the transition structure changes because of the post-wave SBLI, and the stability of ODW is weakened. When the IBL is thick and the equivalence ratio is high, the separation zone is large and the distance between the two separation areas is large, which makes the post-wave

subsonic area merge with the ramp-induced separation, leading to the formation of an extended separation, which covers on the wedge surface in the induction zone. Once the extended separation occurs, the interaction between the pressure rise through the primary transverse wave and the separation expansion makes the separation zone expand further, and finally makes the ODW propagate out of the calculation domain and fail to be stabilized on the wedge.

Funding

This work is supported by National Natural Science Foundation of China (grant numbers 91441101, 51476186).

References

- Ashford, S. A., and G. Emanuel. 1996. Oblique detonation wave engine performance prediction. *J. Propul. Power* 12 (2):322–27.
- [Broda, J. C. 1993. An experimental study of oblique detonation waves. ph.D. thesis, Connecticut Univ.
- Browne, S., J. Ziegler, and J. E. Shepherd. 2004. Numerical solution methods for shock and detonation jump conditions. *Energy Conserv.* 1 (w2):w2.
- Choi, J.-Y., and I.-S. Jeung. 2016. *Numerical simulation of super-detonative ram accelerator; its shock-induced combustion and oblique detonation*. In: Seiler F., Igra O. (eds) Hypervelocity Launchers. Shock Wave Science and Technology Reference Library, vol 10. Springer, Cham.
- Dolling, D. S., and M. T. Murphy. 1983. Unsteadiness of the separation shock wave structure in a supersonic compression ramp flowfield. *AIAA J.* 21 (12):1628–34. doi:10.2514/3.60163.
- [Han, X. 2013. Research on detonation initiation and propagation mechanisms in supersonic premixed flows. ph.D. thesis, Changsha, China, National University of Defense Technology
- Ju, Y., and A. Sasoh. 1997. Numerical study of detonation initiation by a supersonic sphere. *Trans. Jpn. Soc. Aeronaut. Space Sci.* 40 (127):19–29.
- Kailasanath, K. 2000. Review of propulsion applications of detonation waves. *Aiaa J.* 38 (9):1698–708. doi:10.2514/2.1156.
- Kaneshige, M. J., and J. E. Shepherd. 1996. Oblique detonation stabilized on a hypervelocity projectile. *Twenty-Sixth Symp. (Int.) Combust.* 26:3015–22. doi:10.1016/S0082-0784(96)80145-7.
- Kasahara, J., T. Arai, S. Chiba, K. Takazawa, Y. Tanahashi, and A. Matsuo. 2002. Criticality for stabilized oblique detonation waves around spherical bodies in acetylene/oxygen/krypton mixtures. *Proc. Combust. Inst.* 29:2817–24. doi:10.1016/S1540-7489(02)80344-3.
- Lefebvre, M. H., and T. Fujiwara. 1995a. Numerical modeling of combustion processes induced by a supersonic conical blunt body. *Combust. Flame* 100 (1):85–93.
- Lefebvre, M. H., and T. Fujiwara. 1995b. Numerical modeling of combustion processes induced by a supersonic conical blunt body. *Combust. Flame* 100 (1):85–93.
- Li, C., K. Kailasanath, and E. S. Oran. 1993a. Detonation structures behind oblique shocks. *Phys. Fluids* 6 (4):1600–11. doi:10.1063/1.868273.
- [Li, C., K. Kailasanath, and E. S. Oran. 1993b. Effects of boundary layers on oblique-detonation structures. AIAA Paper 1993–0450
- Liu, Y., Y. S. Liu, D. Wu, and J. P. Wang. 2016. Structure of an oblique detonation wave induced by a wedge. *Shock Waves* 26 (2):161–68.
- Liu, Y., L. Wang, B. Xiao, Z. Yan, and C. Wang. 2018. Hysteresis phenomenon of the oblique detonation wave. *Combust. Flame* 192:170–79. doi:10.1016/j.combustflame.2018.02.010.
- Liu, Y., J. Zhou, and Z. Lin. 2014. Ramp-induced oblique detonation wave with an incoming boundary layer effect. *Acta Phys. Sin.* 63 (20):221–28.
- Liu, Y., J. Zhou, and Z. Lin. 2015. Numerical study on the standing morphology of an oblique detonation wave under the influence of an incoming boundary layer. *Open Phys.* 13:15–21.

- Maeda, S., R. Inada, J. Kasahara, and A. Matsuo. 2011. Visualization of the non-steady state oblique detonation wave phenomena around hypersonic spherical projectile. *Proc. Combust. Inst.* 33:2343–49. doi:10.1016/j.proci.2010.06.066.
- Maeda, S., J. Kasahara, and A. Matsuo. 2012. Oblique detonation wave stability around a spherical projectile by a high time resolution optical observation. *Combust. Flame* 159 (2):887–96.
- Maeda, S., S. Sumiya, J. Kasahara, and A. Matsuo. 2013. Initiation and sustaining mechanisms of stabilized oblique detonation waves around projectiles. *Proc. Combust. Inst.* 34:1973–80. doi:10.1016/j.proci.2012.05.035.
- Miao, S., J. Zhou, S. Liu, and X. Cai. 2018. Formation mechanisms and characteristics of transition patterns in oblique detonations. *Acta Astronaut.* 142:121–29. doi:10.1016/j.actaastro.2017.10.035.
- Papalexandris, M. V. 2000. A numerical study of wedge-induced detonations. *Combust. Flame* 120 (4):526–38.
- Silva, L. F. F. D., and B. Deshaies. 2000. Stabilization of an oblique detonation wave by a wedge: a parametric numerical study. *Combust. Flame* 121 (1–2):152–66.
- [Spalart, P., and S. Allmaras. 1992. A one-equation turbulence model for aerodynamic flows. AIAA Paper 92–0439
- Stull, D. R., and H. Prophet. 1971. *JANAF thermodynamical tables*.
- Teng, H. H., and Z. L. Jiang. 2012. On the transition pattern of the oblique detonation structure. *J. Fluid Mech.* 713:659–69. doi:10.1017/jfm.2012.478.
- Teng, H. H., H. D. Ng, and Z. L. Jiang. 2016. Initiation characteristics of wedge-induced oblique detonation waves in a stoichiometric hydrogen-air mixture. *Proc. Combust. Inst.* 36 (2):2735–42.
- Teng, H. H., H. D. Ng, and Z. L. Jiang. 2017. Initiation characteristics of wedge-induced oblique detonation waves in a stoichiometric hydrogen-air mixture. *Proc. Combust. Inst.* 36 (2):2735–42.
- Teng, H. H., Y. N. Zhang, and Z. L. Jiang. 2014. Numerical investigation on the induction zone structure of the oblique detonation waves. *Comput. Fluids* 95:127–31. doi:10.1016/j.compfluid.2014.03.001.
- Teng, H. H., W. Zhao, and Z. L. Jiang. 2007. A novel oblique detonation structure and its stability. *Chin. Phys. Lett.* 24 (7):1985–88. doi:10.1088/0256-307X/24/7/055.
- Valorani, M., M. Digiaccinto, and C. Buongiorno. 2001. Performance prediction for oblique detonation wave engine (ODWE). *Acta Astronaut.* 48 (4):221–28.
- Vasiljev, A. A. 1994. Initiation of gaseous detonation by a high speed body. *Shock Waves* 3:321–26. doi:10.1007/BF01415830.
- Verreault, J., and A. J. Higgins. 2011. Initiation of detonation by conical projectiles. *Proc. Combust. Inst.* 33:2311–18. doi:10.1016/j.proci.2010.07.086.
- Viguier, C., L. F. F. D. Silva, D. Desbordes, and B. Deshaies. 1996. Onset of oblique detonation waves: comparison between experimental and numerical results for hydrogen-air mixtures. *Symp. (Int.) Combust.* 26 (2):3023–31.
- Vlasenko, V. V., and V. A. Sabel'nikov. 1995. Numerical simulation of inviscid flows with hydrogen combustion behind shock waves and in detonation waves. *Combust. Explosion, and Shock Wave* 31 (3):376–89.
- Wang, A. F., W. Zhao, and Z. L. Jiang. 2011. The criterion of the existence or inexistence of transverse shock wave at wedge supported oblique detonation wave. *Acta Mech. Sin.* 27 (5):611–19.
- Wang, T., Y. Zhang, H. Teng, Z. Jiang, and H. D. Ng. 2015. Numerical study of oblique detonation wave initiation in a stoichiometric hydrogen-air mixture. *Phys. Fluids* 27 (9):096101.
- Wolański, P. 2013. Detonative propulsion. *Proc. Combust. Inst.* 34:125–58.
- Yang, P., H. Teng, Z. Jiang, and H. D. Ng. 2018. Effects of inflow mach number on oblique detonation initiation with a two-step induction-reaction kinetic model. *Combust. Flame* 193:246–56. doi:10.1016/j.combustflame.2018.03.026.
- Yang, P. F., H. D. Ng, H. H. Teng, and Z. L. Jiang. 2017. Initiation structure of oblique detonation waves behind conical shocks. *Phys. Fluids* 29:086104. doi:10.1063/1.4999482.
- Yu, M., and S. Miao. 2018. Initiation characteristics of oblique detonation waves in turbulence flows. *Acta Astronaut.* 147:195–204. doi:10.1016/j.actaastro.2018.04.022.